Discovery of Weather in the Oceans –
A Tribute to Prof. Randy Watts

Presented by: Meghan Cronin, URI GSO '93

Now at: NOAA Pacific Marine Environmental Laboratory

Scientific Discovery

is not a simple act, but rather
is an extended, complex process,
which culminates in a

paradigm change

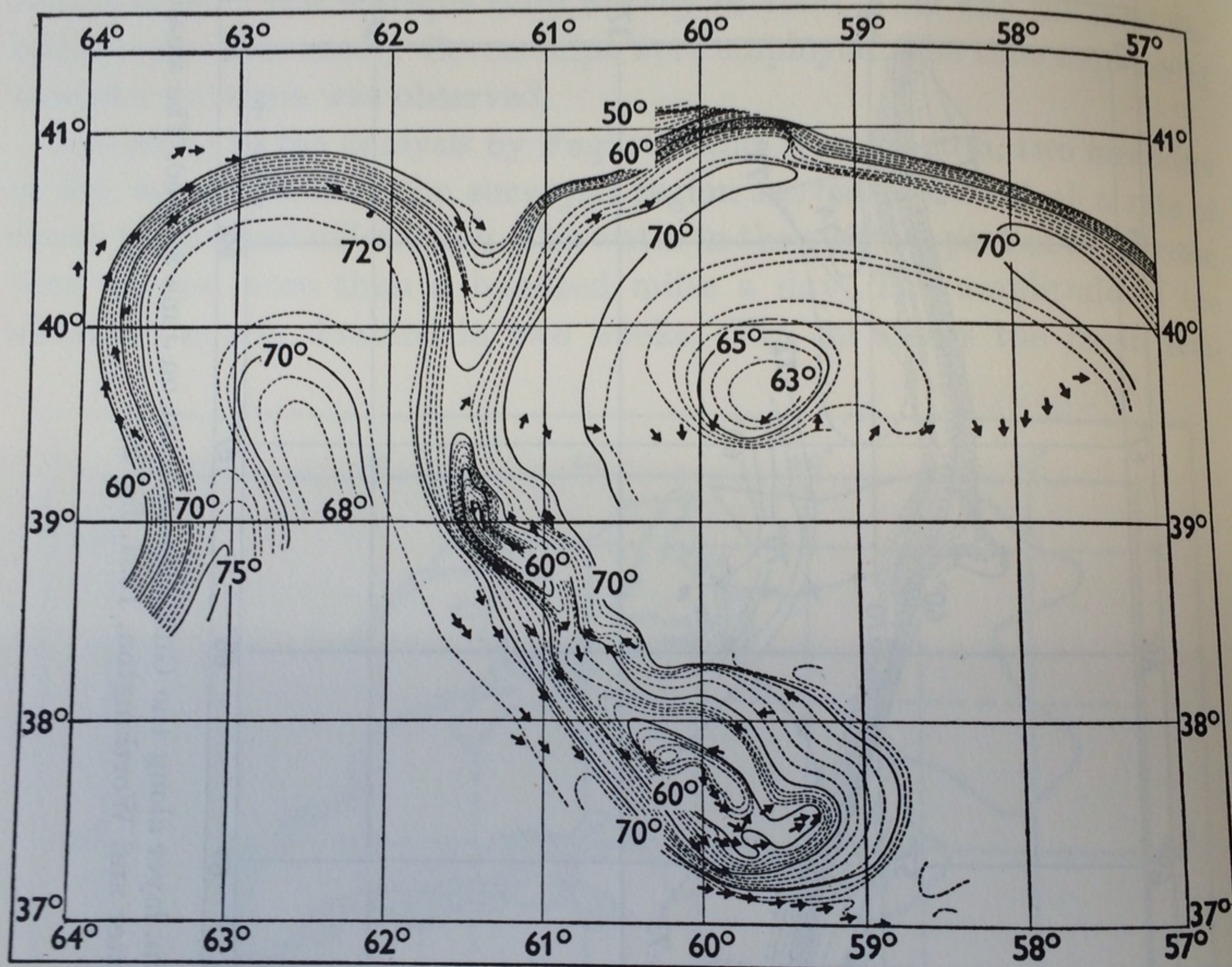

Fig. 30. A continuation of fig. 29 toward the east, showing the large eddy which developed on June 17, 1950 (Fuglister and Worthington, 1951, fig. 7).

From The Gulf Sttream, by Henry Stommel

A. **D. Randolph Watts**

B. **Born December 7, 1943**

C. **Educational History**:

Riverside Polytechnic High School, CA, 1961
B.A., Physics, University of California at Riverside, 1966
Ph.D., Physics, Cornell University, 1973

D. **Professional History prior to coming to URI**:

Feb 1966-Aug 1966 Research Assistant, Physics Dept., University of California at Riverside. Refractory crystal-growth in rare in rare-earth oxides.

Sep 1966-Jun 1968 Teaching Assistant, Physics Dept., Cornell University

Jun 1968-Oct 1972 Research Assistant, Applied Physics Dept., Cornell Univ. Laser light scattering in the superfluid/ normal fluid 3He- 4He mixture.

Nov 1972-Aug 1974 Postdoc, Department of Geology and Geophysics, Yale Inverted Echo Sounder data interpretation in the MODE experiment.

Watts & Rossby, 1977:

Measuring dynamic heights with Inverted Echo Sounders: Results from MODE, *JPO*.

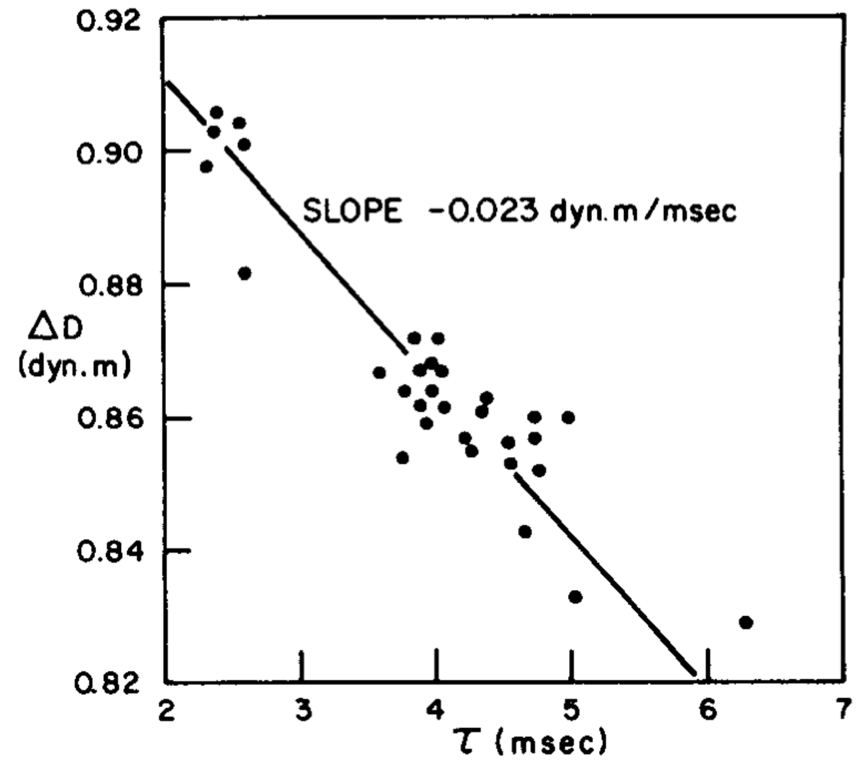

FIG. 4. Acoustic travel times measured by the IES position D (MODE center) plotted against coincident dynamic heights determined from all hydrographic stations taken within 20 km of that site. Travel times τ are in milliseconds after a constant 7.1993 s has been subtracted. Dynamic heights are calculated for the pressure interval, 500 to 1500 db, spanning the main thermocline. The line with the least square error in τ is shown.

APPENDIX I

3. MODE-I SHIP SCHEDULE 1973

	MARCH				APRIL					MAY				JUNE				JULY			
WEEKENDS	4	11	18	25	1	8	15	22	29	6	13	20	27	3	10	17	24	1	8	15	22

density

30

30

t.

FL

22

Chaplin & Watts, 1984:

Inverted Echo Sounder Development, *IEEE*.

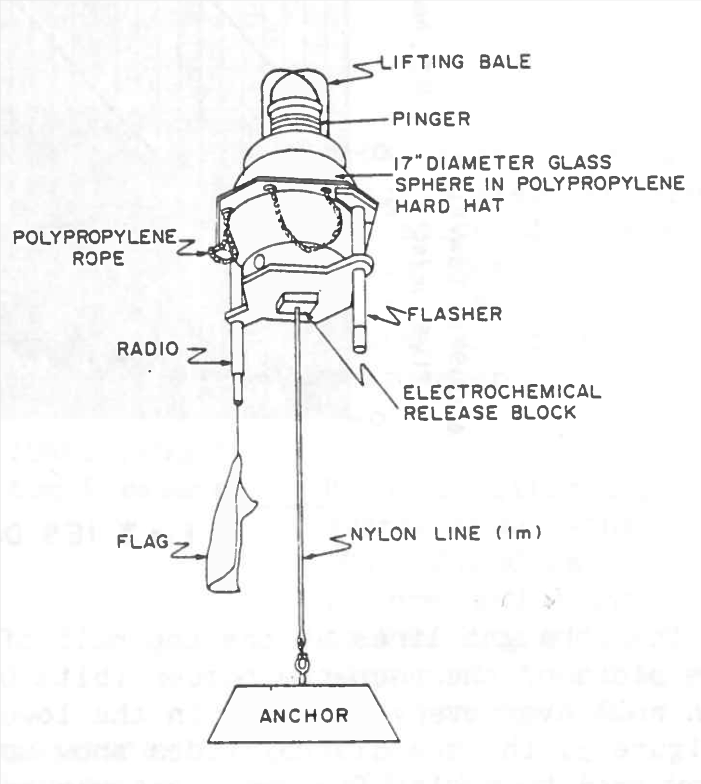

Fig.2 Diagram of Moored IES.

An IES *measures round-trip travel time for pings to go from ocean bottom, to surface, and back... Very accurately.*

Tracey and Watts, 1986:
On Gulf Stream Meander Characteristics Near Cape Hatteras, *JGR*.

TRACEY AND WATTS: GULF STREAM MEANDERS OFF CAPE HATTERAS

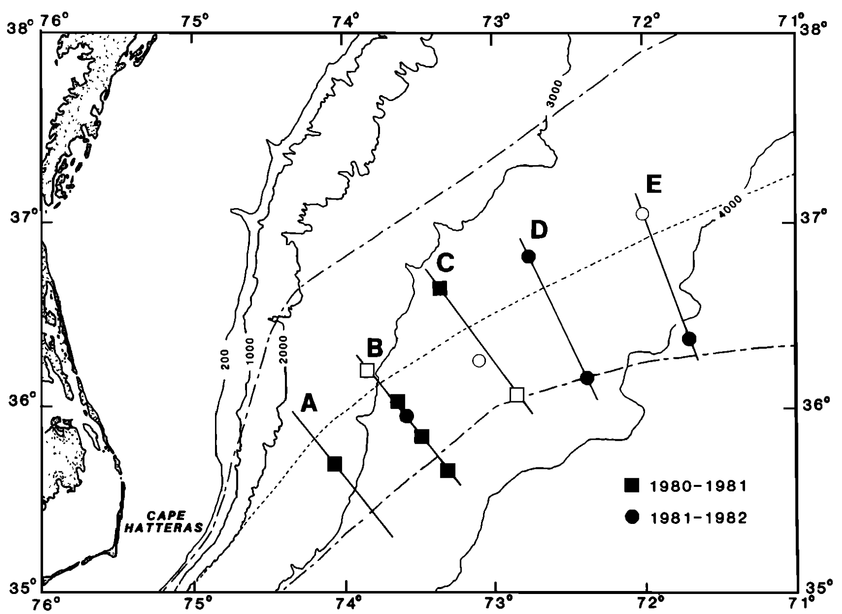

Fig. 1. Study area. IES sites are shown for the 1980–1981 (squares) and 1981–1982 (circles) deployment periods along lines A–E. Open symbols indicate sites where no data were collected due to data tape failures or instrument losses; solid symbols are sites with data. The historical mean location of the north wall is shown by the center dashed line, and the "90% envelope" (see text) is delineated by the upper and lower long-short dashed lines.

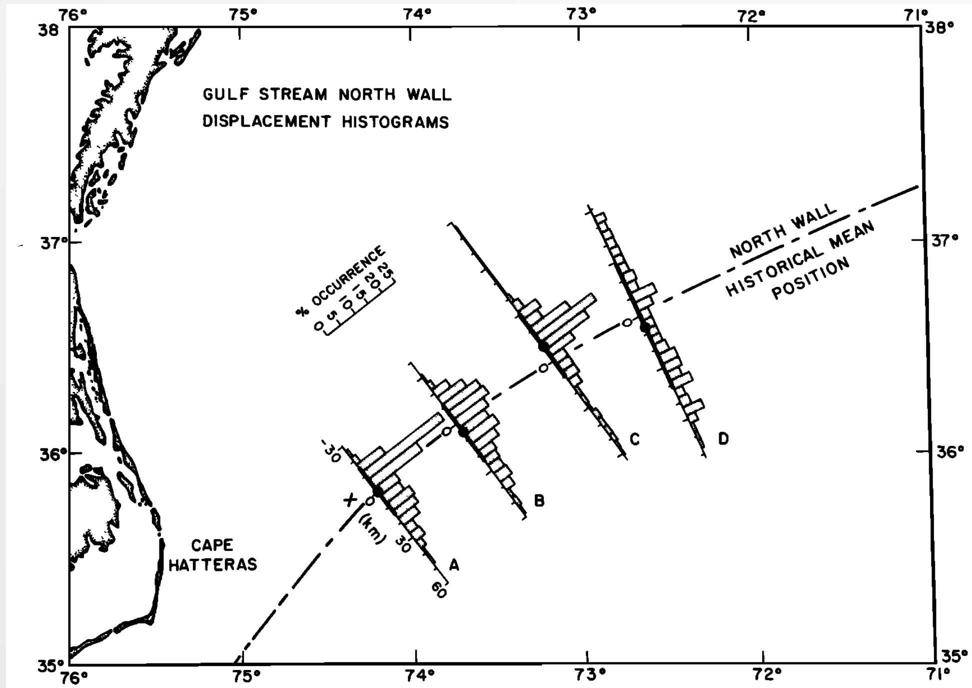

Fig. 5. Histograms of north wall position along lines A–D shown as percent occurrence. Means and standard deviations are shown by the large solid dots and heavy bars, respectively. The lateral scale on line A applies to all lines.

E.M. Johns, Watts, & Rossby, 1989: A test of geostrophy in the Gulf Stream, *JGR.*

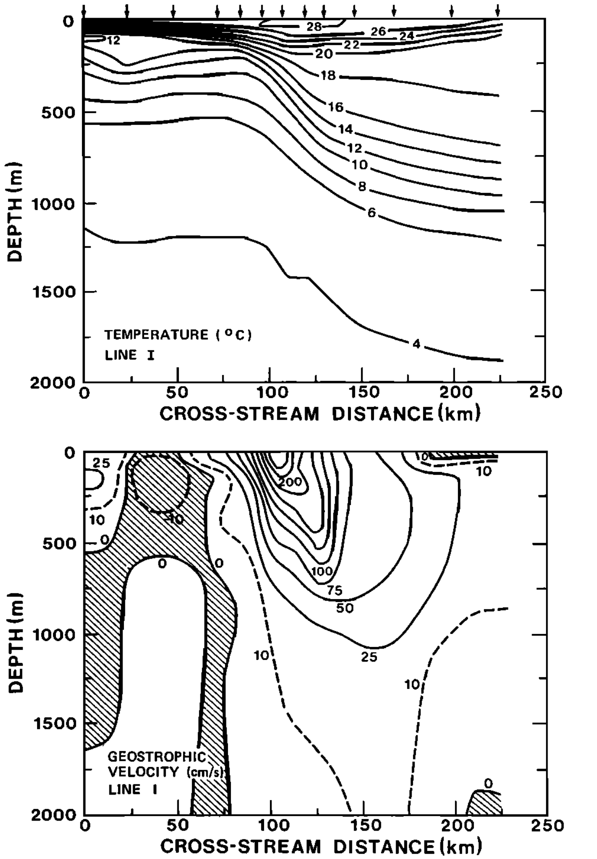

Fig. 4. (*a*) Cross section of temperature (in degrees Celsius) from the first survey (line I). CTD station locations are shown by arrows across the top of the figure. (*b*) Cross section of geostrophic velocity v_g (in centimeters per second) for line I, referenced at 2000 m to agree with the Pegasus velocity.

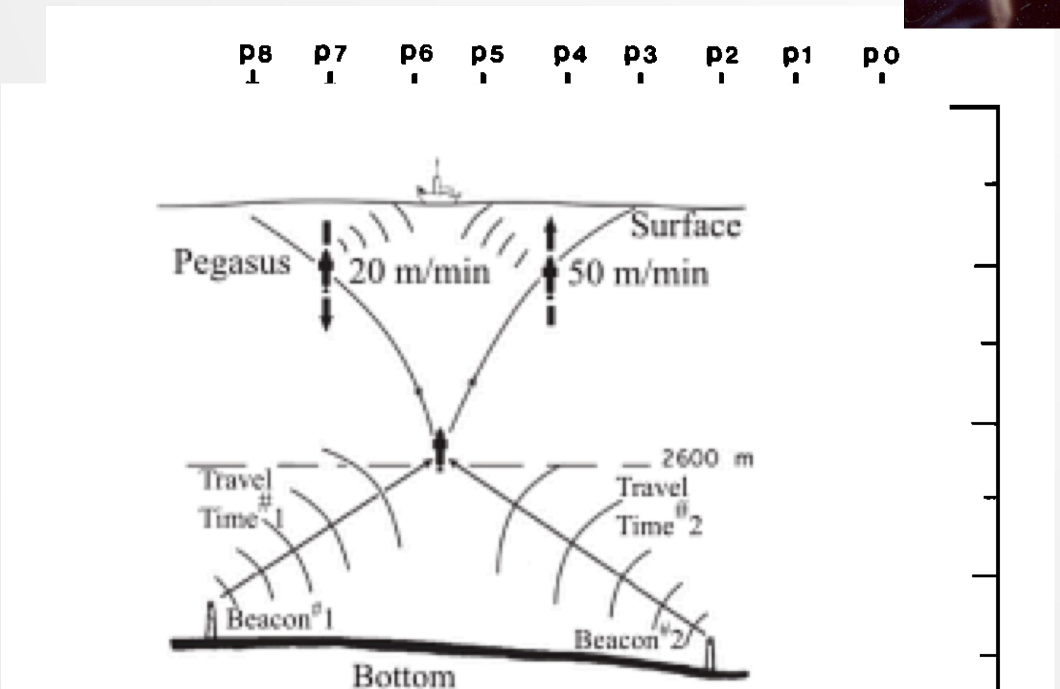

FIGURE 10.25 Schematic diagram showing acoustic tracking of free-falling current velocity profiler (Pegasus) relative to two expendable beacons. (*Source: Spain et al., 1981.*)

Fig. 6. Cross section of the difference between the absolute and geostrophic velocity, $\Delta v = v_p - v_g$, for line I. The nine Pegasus sites are indicated by arrows.

Manning and Watts, 1989:

Temperature and velocity structure of the Gulf Stream northeast of Cape Hatteras: Principal modes of variability, *JGR*.

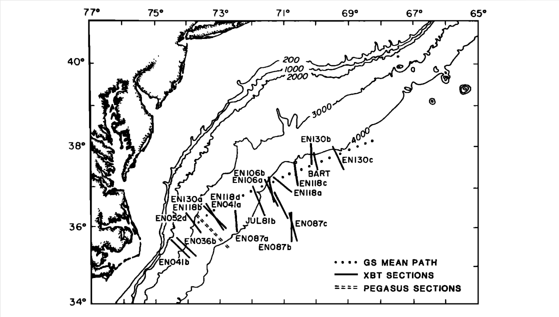

Fig. 1. Study area and transect locations. The solid lines indicate XBT sections and the double dashed line indicates Pegasus sections. Bathymetric contours are in meters, and cruise numbers are listed. The mean path of the north wall of the Gulf Stream is indicated.

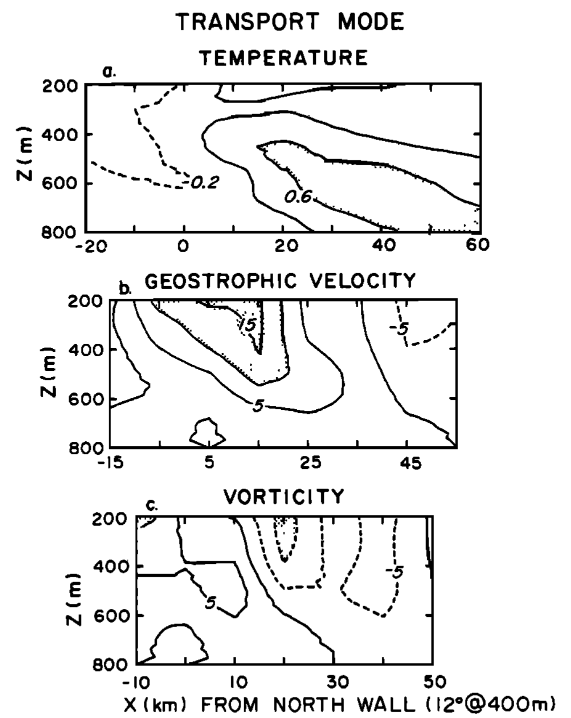

Fig. 6. The transport mode from 19 temperature sections {T19} that exclude the Pegasus section: (a) temperature with 0.4°C contour interval, (b) geostrophic velocity with 5 cm s^{-1} contour interval, and (c) associated vorticity with 1 x 10^{-6} s^{-1} contour interval.

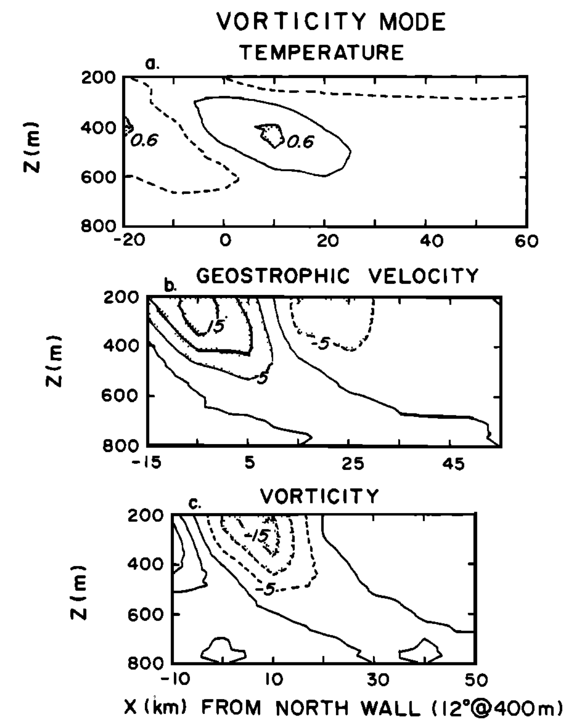

Fig. 8. The vorticity mode from 35 temperature sections below 200 m. The second temperature mode is associated with a large perturbation of the lateral shear in geostrophic velocity near the core of the Gulf Stream. The stippled region indicates (a) deviations in temperature greater than 0.6°C, (b) deviations in geostrophic velocites of greater than 5 cm s^{-1}, and (c) deviations in vorticity greater than 10 x 10^{-6} s^{-1}.

Kontoyiannis & Watts, 1994:

Observations on the variability of the Gulf Stream path between 74W and 70W, *JPO*.

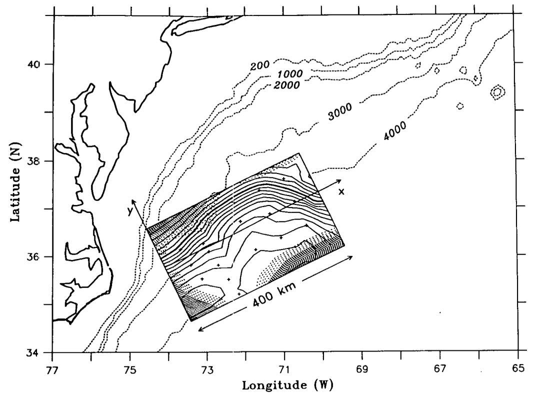

FIG. 1. Study area, shown within the rectangle, and coordinate system. Within our study area, we show as an example the objective analysis map of Z_{12}, the depth of the 12°C isothermal surface, during 27 May 1984; Z_{12} is contoured at 50-m intervals and shoals to the north. The thick line shows the subsurface path where 12°C crosses 400-m depth. The objective analysis is based on IES data from sites marked with +. The x axis is oriented 064°T, approximately along the mean path of the Gulf Stream in this area. Shading corresponds to regions of error ≥15%.

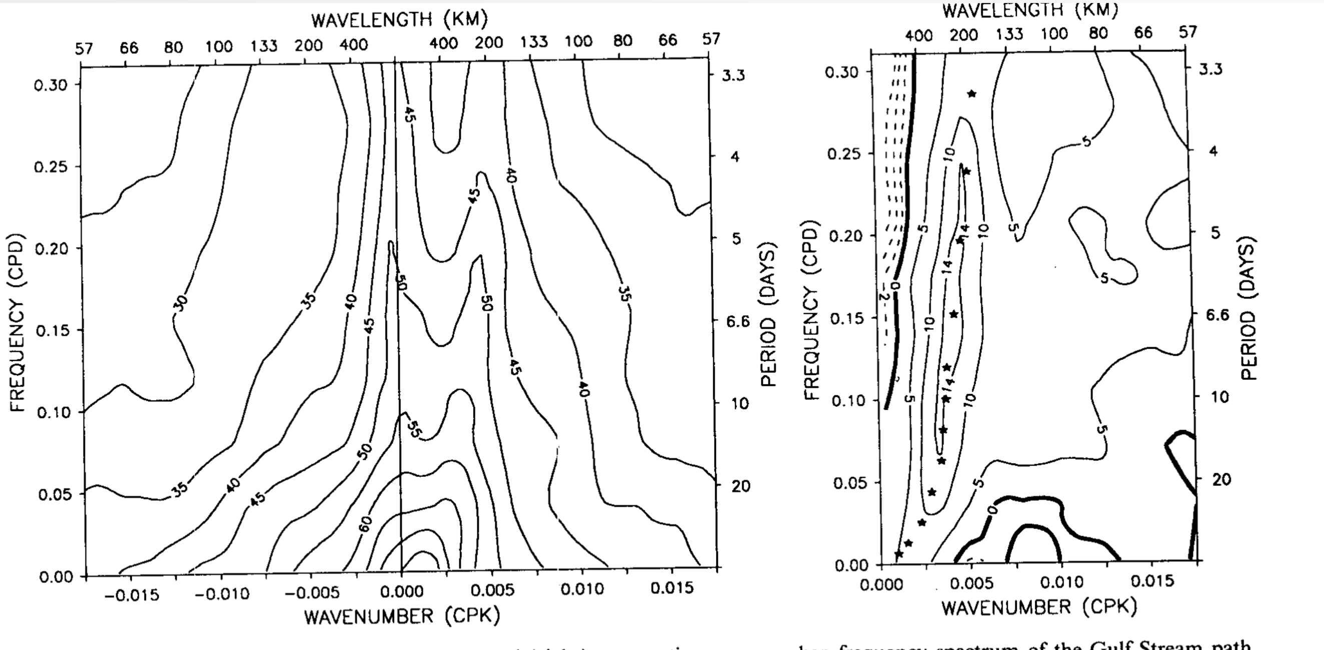

FIG. 6. (Left) Wavenumber–frequency spectrum and (right) propagating wavenumber–frequency spectrum of the Gulf Stream path. Contoured in the wavenumber–frequency spectrum is PSD in dB relative to 1 km^2 cpd^{-1} cpk^{-1}. The propagating spectrum is the difference between the right and the left quadrant of the wavenumber–frequency spectrum. The stars superposed on the right panel are the dispersion relation (frequency vs wavenumber) of downstream propagating meanders determined from the EOF analysis on the Gulf Stream path. Note in right panel that for negative values the contour interval changes to −2 dB. The AR model order is 9.

Johns, W.E. and Watts, 1985:
Gulf Stream Meanders: observations on the deep currents, *JGR*.

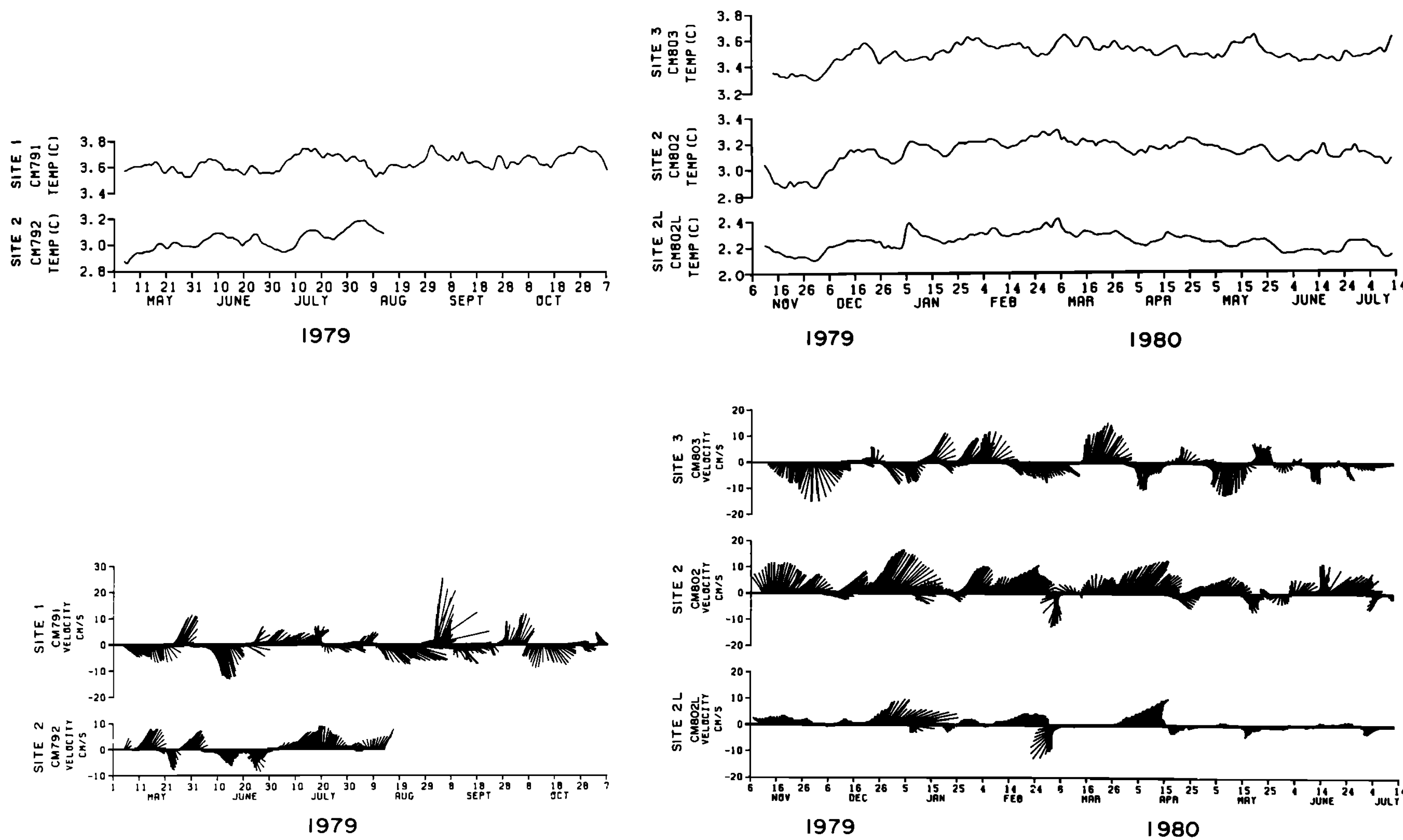

Fig. 2. Time series of velocity (lower panels) and temperature (upper panels) for sites 1, 2, 2L, and 3 for May–November 1979 and November 1979 to July 1980. North is upward.

SYNOP: May 1988-August 1990

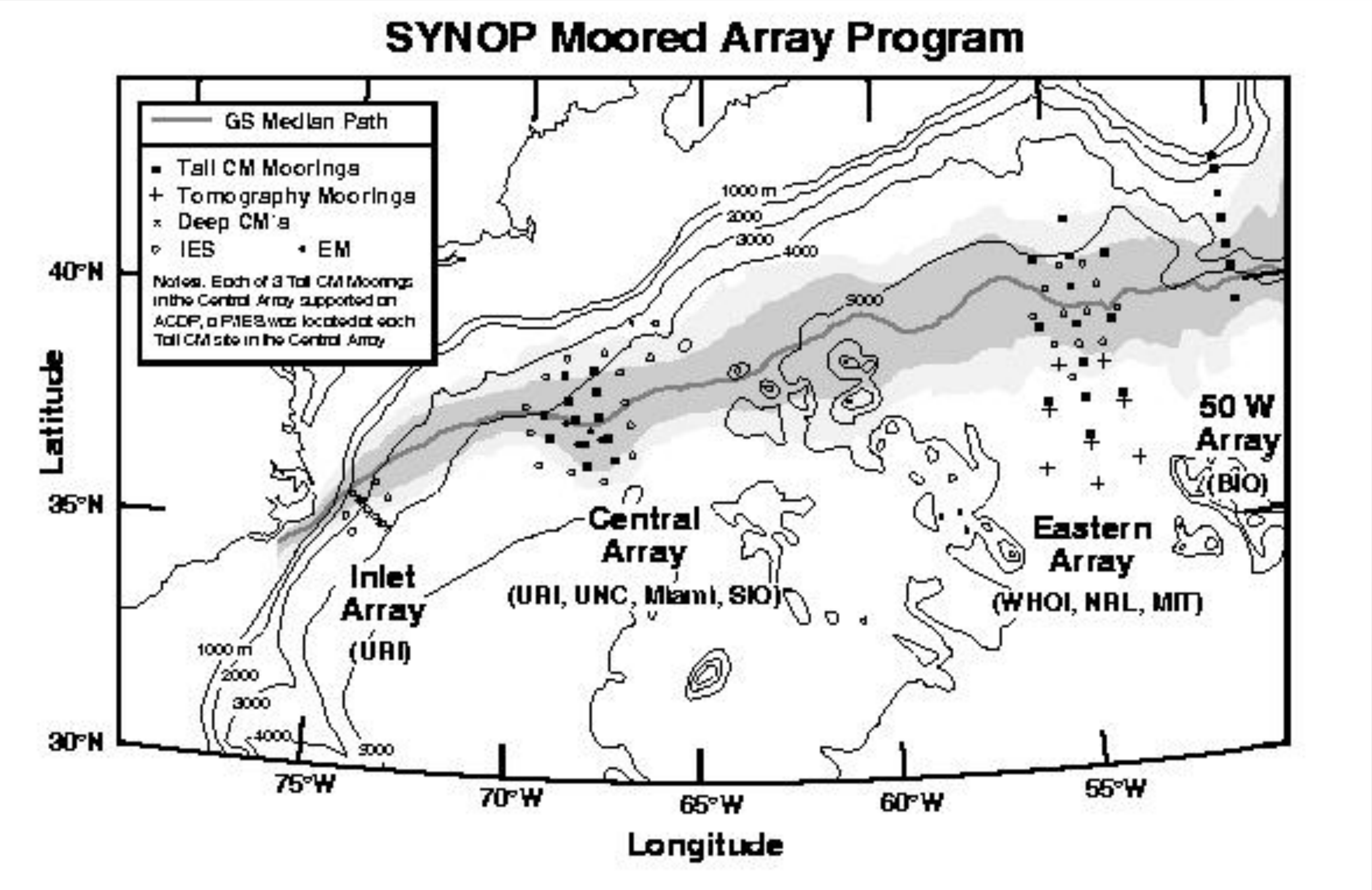

INTERNATIONAL GEOPHYSICS SERIES • VOLUME 23

An Introduction to Dynamic Meteorology

Second Edition

James R. Holton

6.2.3 The Quasi-Geostrophic Potential Vorticity Equation

The geopotential tendency equation which we discussed in the previous subsection may be regarded as a diagnostic equation which relates $\chi \equiv \partial\Phi/\partial t$ to the distribution of Φ. The form of this equation given in (6.14) is ideal for discussing the physical processes which generate the geopotential tendency field. However, since the tendency is just the local time rate of change of geopotential (6.14) can also be regarded as a *prognostic* equation for the time evolution of the Φ field. To use (6.14) prognostically it is convenient to simplify the right-hand side by using the chain rule of differentiation to write term C as

$$-\frac{f_0^2}{\sigma}\mathbf{V}_g\cdot\nabla\frac{\partial^2\Phi}{\partial p^2}-\frac{f_0^2}{\sigma}\frac{\partial\mathbf{V}_g}{\partial p}\cdot\nabla\frac{\partial\Phi}{\partial p} \qquad (6.16)$$

But $f_0\partial\mathbf{V}_g/\partial p = \mathbf{k}\times\nabla(\partial\Phi/\partial p)$, which is perpendicular to $\nabla(\partial\Phi/\partial p)$. Thus, the second part of (6.16) vanishes and the first part can be combined with term B in (6.14) to yield

$$\left(\frac{\partial}{\partial t}+\mathbf{V}_g\cdot\nabla\right)\left[\frac{1}{f_0}\nabla^2\Phi+f+\frac{f_0}{\sigma}\frac{\partial^2\Phi}{\partial p^2}\right]=0 \qquad (6.17)$$

This equation can be written in a more compact form as

$$\frac{Dq}{Dt}=0$$

$$q\equiv\frac{1}{f_0}\nabla^2\Phi+f+\frac{f_0}{\sigma}\frac{\partial^2\Phi}{\partial p^2},\qquad \frac{D}{Dt}\equiv\frac{\partial}{\partial t}+\mathbf{V}_g\cdot\nabla \qquad (6.18)$$

Thus, the scalar quantity q is conserved following the geostrophic wind in isobaric coordinates. The scalar q, often called the *quasi-geostrophic potential vorticity*, is a linearized form of the potential vorticity $(\zeta+f)\,\partial\theta/\partial p$ discussed in Section 4.3. Given the distribution of Φ, (6.18) can be integrated in time to provide a forecast of the evolution of the Φ field. However, because V_g depends on the distribution of Φ the equation is highly nonlinear and numerical methods must be used for obtaining solutions.

6.2.4 The Omega Equation

A diagnostic equation for the vertical motion field may be obtained by eliminating χ between (6.12) and (6.13). To do this, we take the horizontal Laplacian of (6.12) to obtain

$$\nabla^2\frac{\partial\chi}{\partial p}=-\nabla^2\left[\mathbf{V}_g\cdot\nabla\left(\frac{\partial\Phi}{\partial p}\right)\right]-\sigma\nabla^2\omega \qquad (6.19)$$

where we have again assumed that σ is a constant. We next differentiate (6.13) with respect to pressure yielding

$$\frac{\partial}{\partial p}(\nabla^2\chi)=-f_0\frac{\partial}{\partial p}\left[\mathbf{V}_g\cdot\nabla\left(\frac{1}{f_0}\nabla^2\Phi+f\right)\right]+f_0^2\frac{\partial^2\omega}{\partial p^2} \qquad (6.20)$$

Since the order of the operators on the left-hand side in (6.19) and (6.20) may be reversed, the result of subtracting (6.19) from (6.20) is to eliminate χ. After some rearrangement of terms, we obtain the *omega equation*

$$\underbrace{\left(\nabla^2+\frac{f_0^2}{\sigma}\frac{\partial^2}{\partial p^2}\right)\omega}_{\text{A}}=\underbrace{\frac{f_0}{\sigma}\frac{\partial}{\partial p}\left[\mathbf{V}_g\cdot\nabla\left(\frac{1}{f_0}\nabla^2\Phi+f\right)\right]}_{\text{B}}+\underbrace{\frac{1}{\sigma}\nabla^2\left[\mathbf{V}_g\cdot\nabla\left(-\frac{\partial\Phi}{\partial p}\right)\right]}_{\text{C}} \qquad (6.21)$$

Equation (6.21) involves only derivatives in space. It is, therefore, a diagnostic equation for the field of ω in terms of the instantaneous Φ field. The omega equation, unlike the continuity equation, gives a measure of ω which does not depend on accurate observations of the horizontal wind. In fact, direct wind observations are not required at all. This method is also superior to the vorticity equation method since no knowledge of the vorticity tendency is required. In fact, only observations of Φ at a single time are required to determine the ω field using (6.21).

As was the case for the geopotential tendency equation, the terms in (6.21) are all subject to straightforward physical interpretation. The differential operator in A is identical to the operator in term A of the tendency equation (6.14). Assuming that ω has a horizontal spatial dependence similar to that of χ and a vertical dependence similar to that of $\partial\chi/\partial p$, i.e.,

$$\omega=\sin(\pi p/p_0)\sin kx\sin ly$$

we can write

$$\left(\nabla^2+\frac{f_0^2}{\sigma}\frac{\partial^2}{\partial p^2}\right)\omega\simeq\left[-(k^2+l^2)-\frac{1}{\sigma}\left(\frac{f_0\pi}{p_0}\right)^2\right]\omega$$

from which we can see that term A is proportional to $-\omega$.

Term B is called the *differential vorticity advection.* Clearly this term is proportional to the rate of increase with height of the advection of absolute vorticity. To understand the role of differential vorticity advection we again consider an idealized developing baroclinic system. Figure 6.9 indicates schematically the geopotential contours at 500 and 1000 mb for such a system. At the centers of the surface high and surface low, designated H and L, respectively, the vorticity advection at 1000 mb must be very small. However, at 500 mb the positive relative vorticity advection is a *maximum* above

Lindstrom & Watts, 1994:

Vertical motion in the Gulf Stream near 68W, *JPO*.

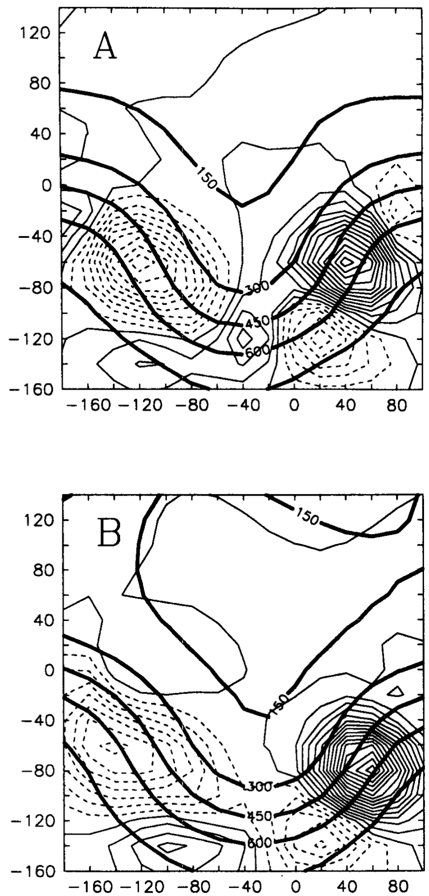

FIG. 11. Mapped thermocline topography—that is, z_{12}—(bold, contour interval 150 m) as measured by IES, overlain by w_{IES} computed from (4) (contour interval 0.25 mm s^{-1}, negative values dashed), (a) at 1200 UTC 19 May 1990 and (b) at 1200 UTC 27 May 1990. Note the stationarity of features. The maximum in downward vertical motion at (−120, −70) is also captured in the CM data for G3 (not shown).

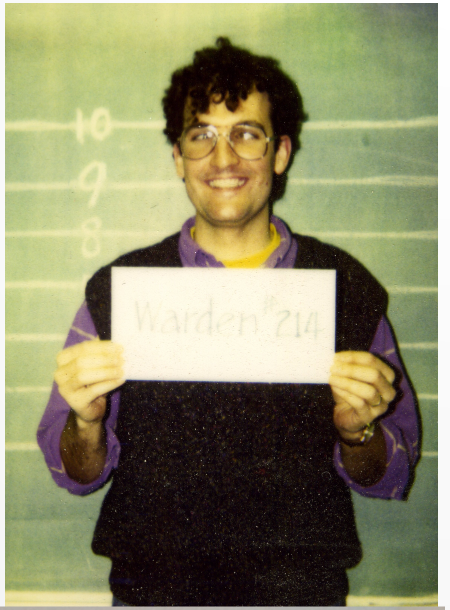

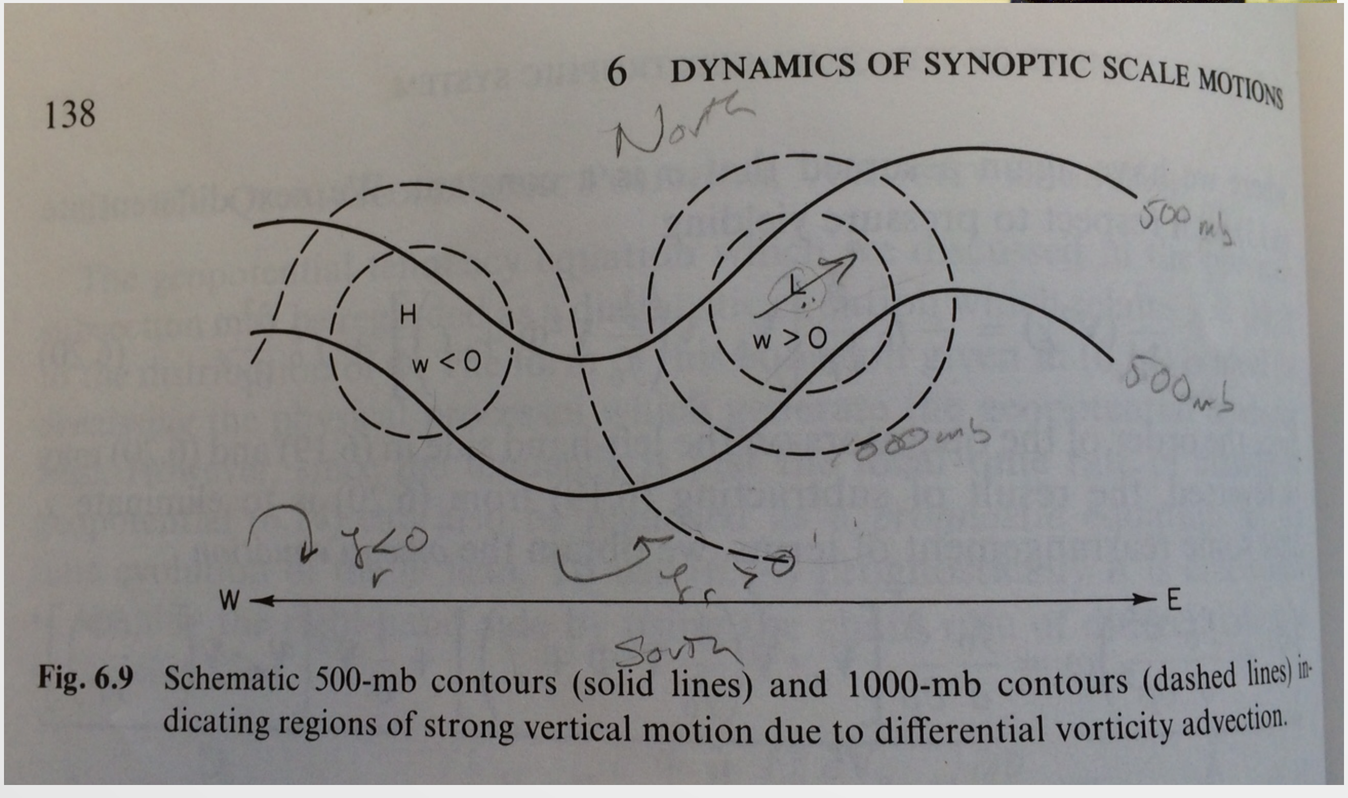

138 6 DYNAMICS OF SYNOPTIC SCALE MOTIONS

Fig. 6.9 Schematic 500-mb contours (solid lines) and 1000-mb contours (dashed lines) indicating regions of strong vertical motion due to differential vorticity advection.

Watts, Tracey, Bane, & Shay, 1995: Gulf Stream path and thermocline structure near 74W and 68W, *JGR*.

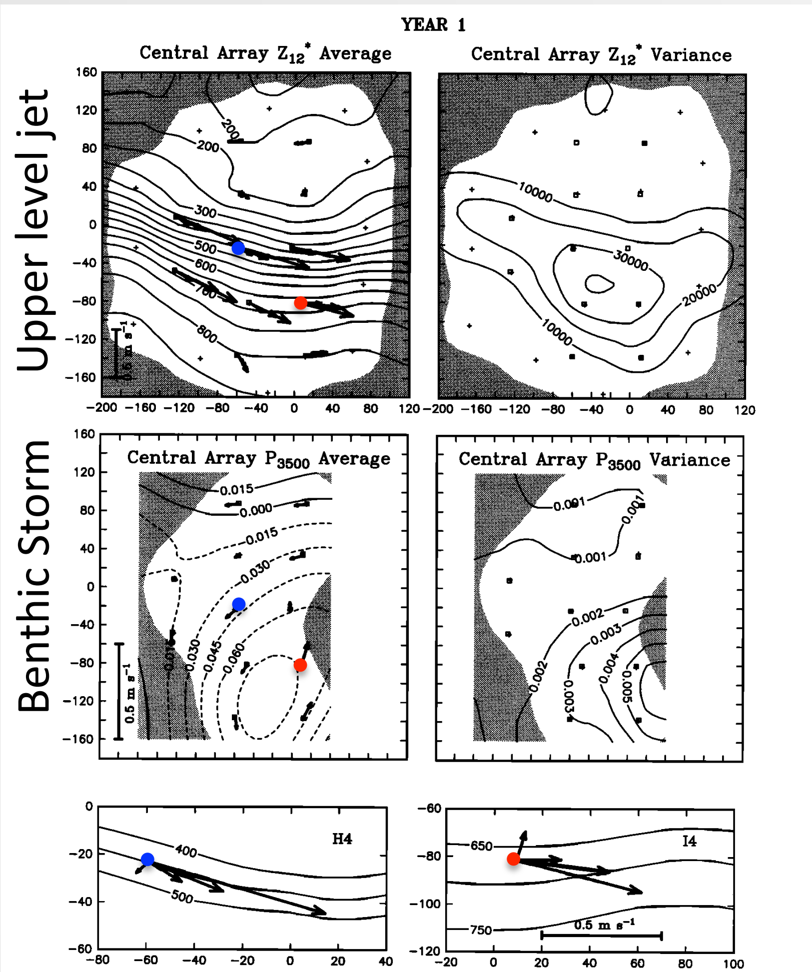

Backing current

Veering current

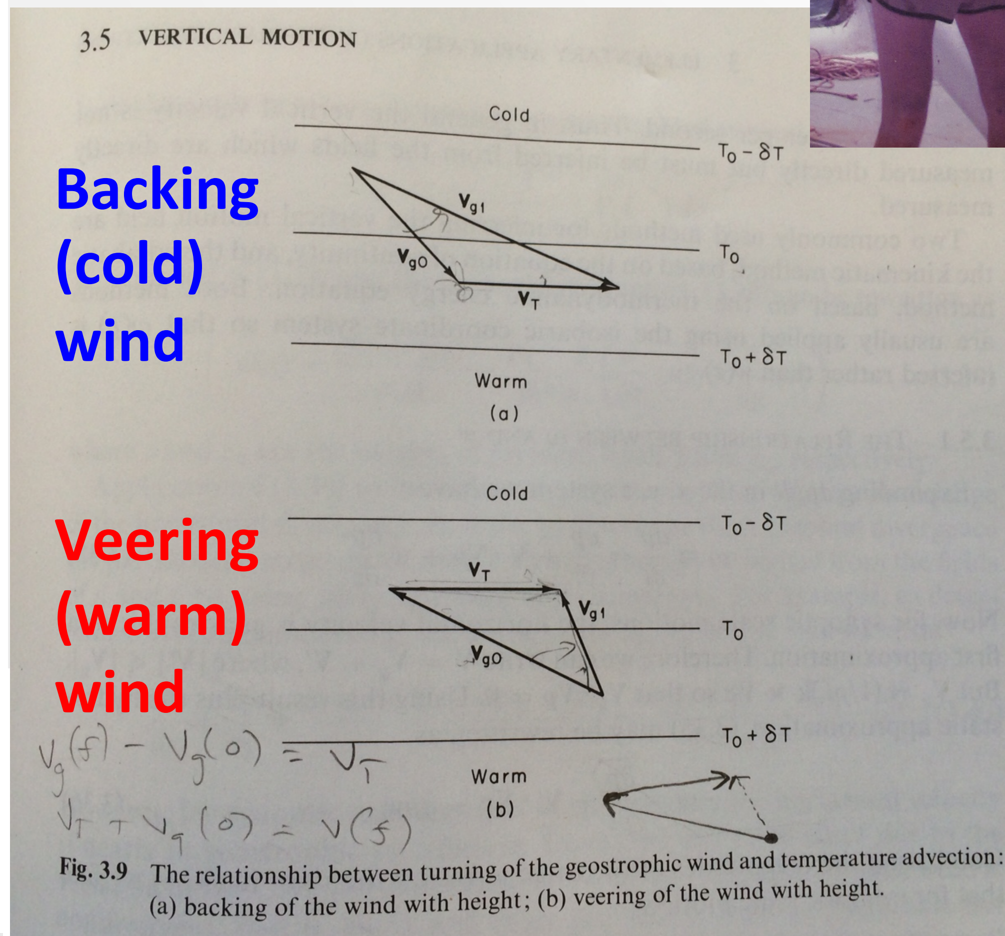

Backing (cold) wind

Veering (warm) wind

Donohue et al., 2010: Mapping circulation in the Kuroshio Extension with an array of current and pressure recording inverted echo sounders, *JAOT*.

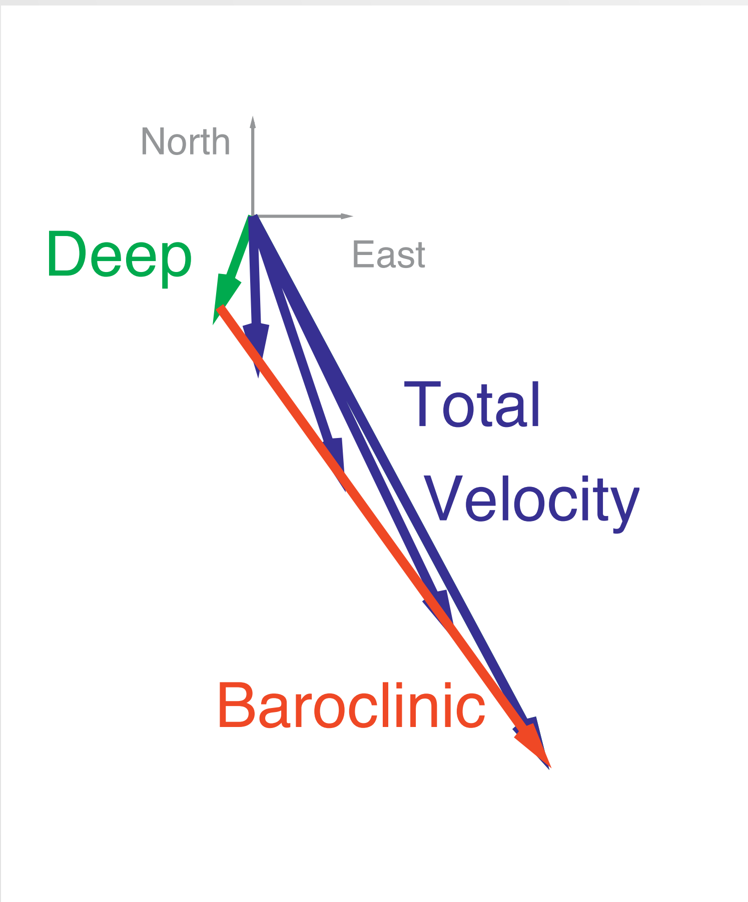

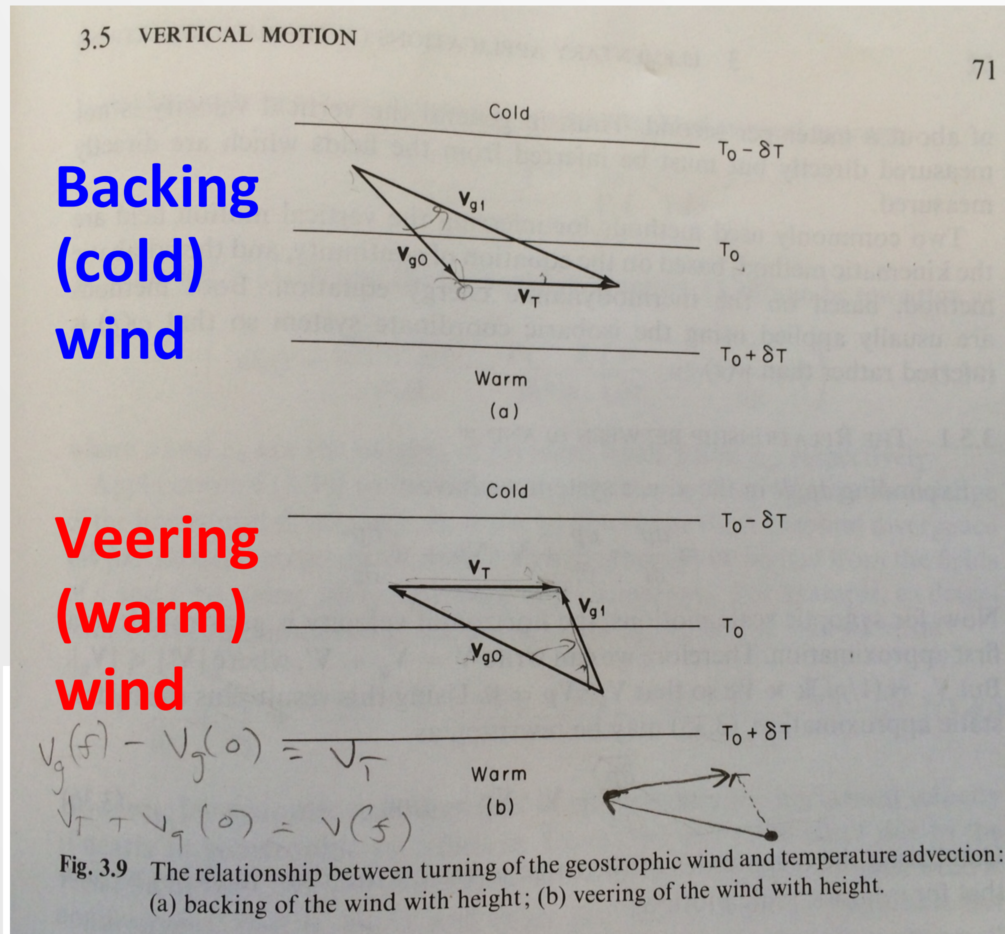

Cronin & Watts, 1996: Eddy-mean flow interation in the Gulf Stream at 68W: Part I. Eddy energetics, *JPO*.

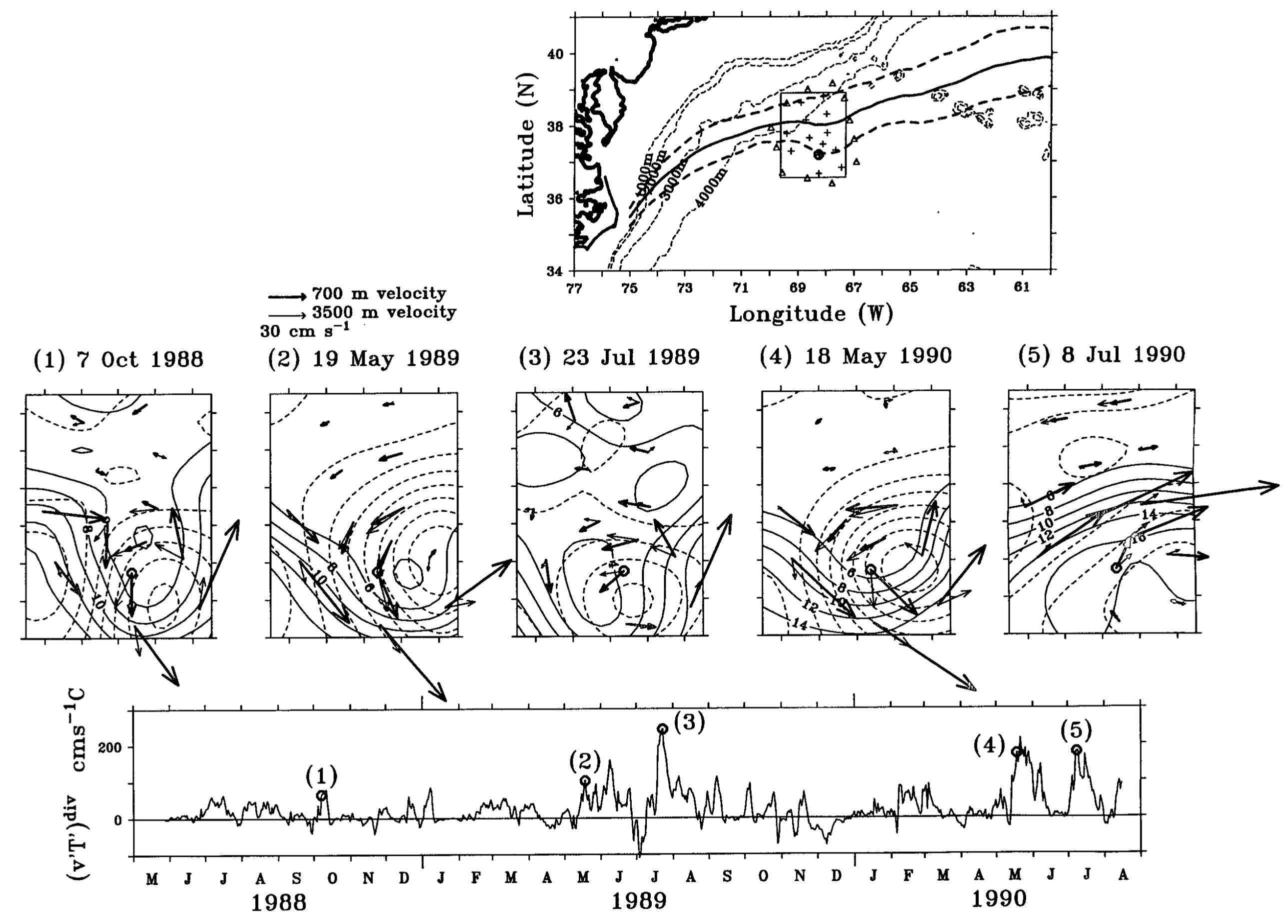

FIG. 16. The 700-m level $(v'T')^{div}$ time series at mooring site H5 (shown as an open circle in the maps). The selected instantaneous maps show the velocity vectors at 700 m (dark vectors) and 3500 m (light vectors) superimposed on the 700-m temperature field (solid contours) and 3500-m streamlines (dashed contours). Major peaks in the $(v'T')^{div}$ time series can be associated with baroclinic instability events illustrated in the selected maps. The prevalence of trough events in the study region results in a weak trough feature in the long-term mean Gulf Stream path (see Fig. 1).

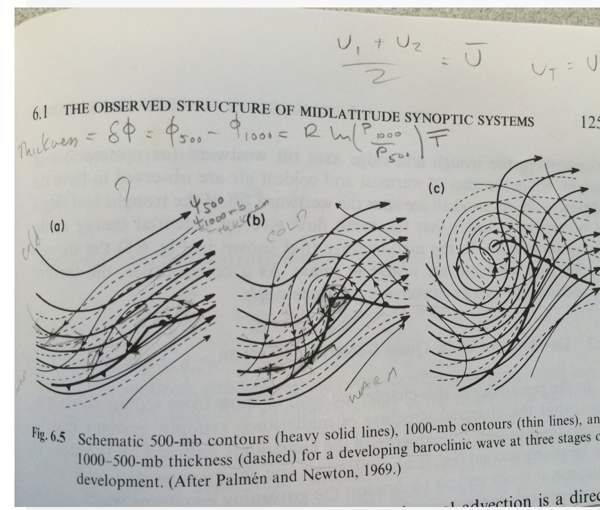

6.1 THE OBSERVED STRUCTURE OF MIDLATITUDE SYNOPTIC SYSTEMS 125

Fig. 6.5 Schematic 500-mb contours (heavy solid lines), 1000-mb contours (thin lines), and 1000–500-mb thickness (dashed) for a developing baroclinic wave at three stages of development. (After Palmén and Newton, 1969.)

...advection is a direct

Howden & Watts, 1999:

Jet streaks in the Gulf Stream, *JPO*.

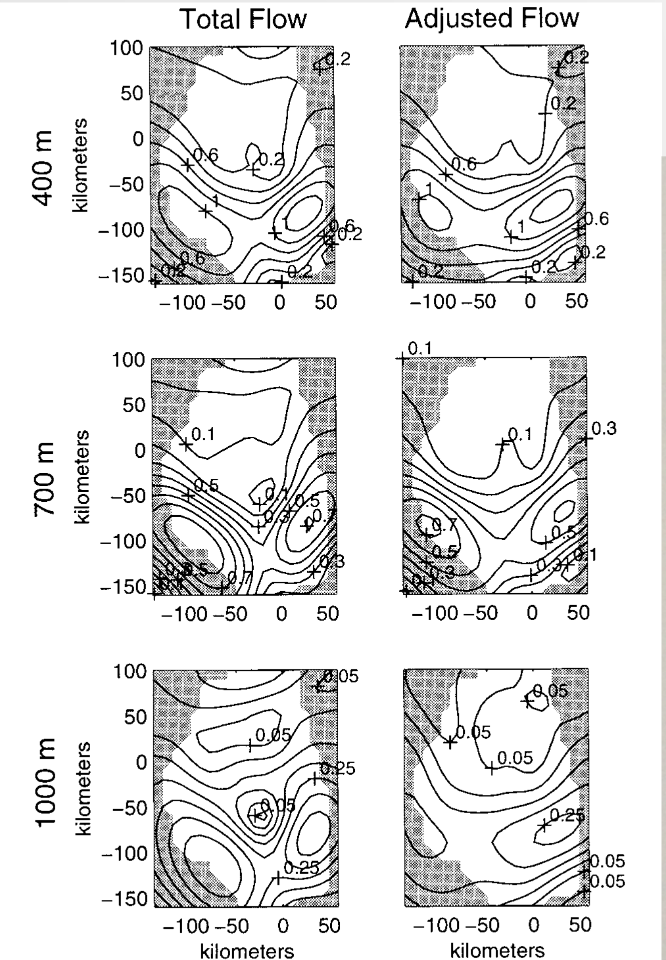

FIG. 5. The first column shows the isotach structure at depths 400, 700, and 1000 m on 29 September 1988. The second column shows the isotachs of the residual flow V_R on the same date for the same sets of depths.

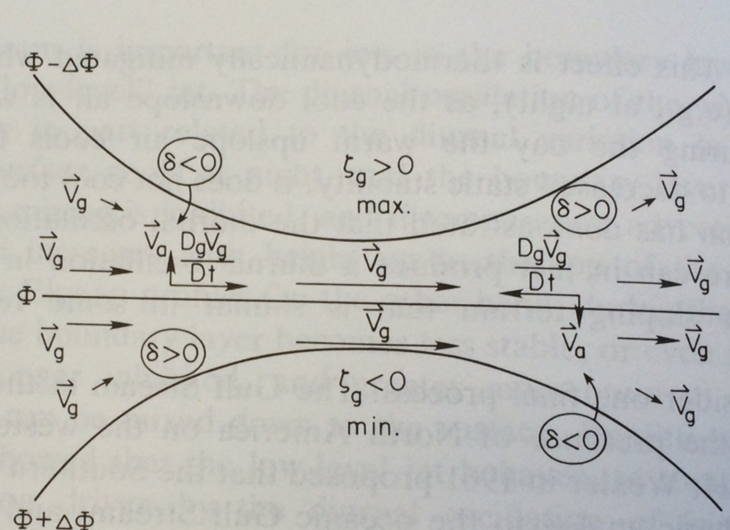

Figure 2.100 Parcel dynamics in a jet streak. Geopotential-height contours Φ (solid lines); $\mathbf{v}_g$ represents the geostrophic wind; $\mathbf{v}_a$ represents the ageostrophic wind, which in this Northern Hemisphere example is oriented perpendicular and to the left of the geostrophic parcel acceleration vector $D_g\mathbf{v}_g/Dt$. There is convergence ($\delta < 0$) in the right-front and left-rear quadrants; there is divergence ($\delta > 0$) in the left-front and right-rear quadrants. A maximum (minimum) in shear and curvature vorticity are found just to the left (right) of the jet streak.

Kim and Watts, 1994:
An observational stream function in the Gulf Stream, *JPO*.

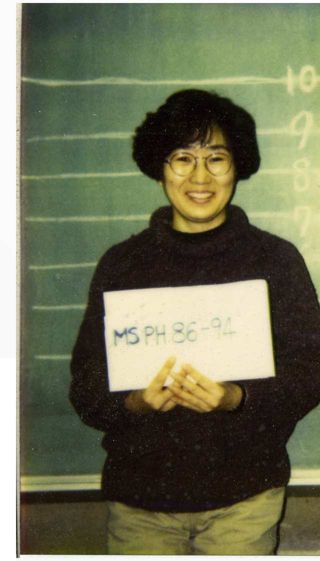

now examine, respectively, the gradient ∇ and the Laplacian ∇^2 operators, which are each subject to two types of error, "numerical error" and "measurement and statistical error," as briefly mentioned in the introduction. We summarize both error sources here. This guides our choice of the best grid spacing for each differential operator.

a. Error estimates and minimization for geostrophic velocities

On a uniform grid of points separated by distance Δ, the centered difference formula of velocity $\mathbf{V}_\psi = -\psi_y \mathbf{i} + \psi_x \mathbf{j}$ expressed in x, y components at point (i, j) is

$$\mathbf{V}_\psi = -\left\{\frac{\psi(i, j+\Delta) - \psi(i, j-\Delta)}{2\Delta} - \frac{\Delta^2}{6}\psi_{yyy}(i, \eta)\right\}\mathbf{i} + \left\{\frac{\psi(i+\Delta, j) - \psi(i-\Delta, j)}{2\Delta} - \frac{\Delta^2}{6}\psi_{xxx}(\xi, j)\right\}\mathbf{j}, \quad (4)$$

where ψ_{xxx} and ψ_{yyy} represent the maximum values of the third-order derivatives of ψ with respect to x and y for the ranges $i - \Delta \leqslant \xi \leqslant i + \Delta$ and $j - \Delta \leqslant \eta \leqslant j + \Delta$. The terms on the rhs, which include ψ_{xxx} and ψ_{yyy}, are the standard numerical truncation errors (generally of unknown sign) that arise from centered finite differencing (Ames 1977). The vector component errors are independent, and the numerical error $\mathcal{N}_{\mathbf{V}_\psi}$ may be expressed as

$$\mathcal{N}_{\mathbf{V}_\psi} = \begin{bmatrix} \frac{\Delta^2}{6}\psi_{yyy}(i, \eta) \\ -\frac{\Delta^2}{6}\psi_{xxx}(\xi, j) \end{bmatrix}. \quad (5)$$

$$e_{\psi_x} = \frac{1}{2\Delta}[\{\psi(i+\Delta, j) - \hat{\psi}(i+\Delta, j)\} - \{\psi(i-\Delta, j) - \hat{\psi}(i-\Delta, j)\}] = \frac{1}{2\Delta}[e(i+\Delta, j) - e(i-\Delta, j)].$$

Expanding the linear operator E on variance of the component $e_{\psi_x} e_{\psi_x}$,

$$E[e_{\psi_x} e_{\psi_x}] = \frac{1}{(2\Delta)^2}\begin{pmatrix} E[e(i+\Delta, j)e(i+\Delta, j)] \\ -E[e(i-\Delta, j)e(i+\Delta, j)] \\ -E[e(i+\Delta, j)e(i-\Delta, j)] \\ +E[e(i-\Delta, j)e(i-\Delta, j)] \end{pmatrix}.$$

It may be rewritten, using the shorthand notation of

He & Watts, 1998:

Determining geostrophic velocity shear profiles with IES, JGR.

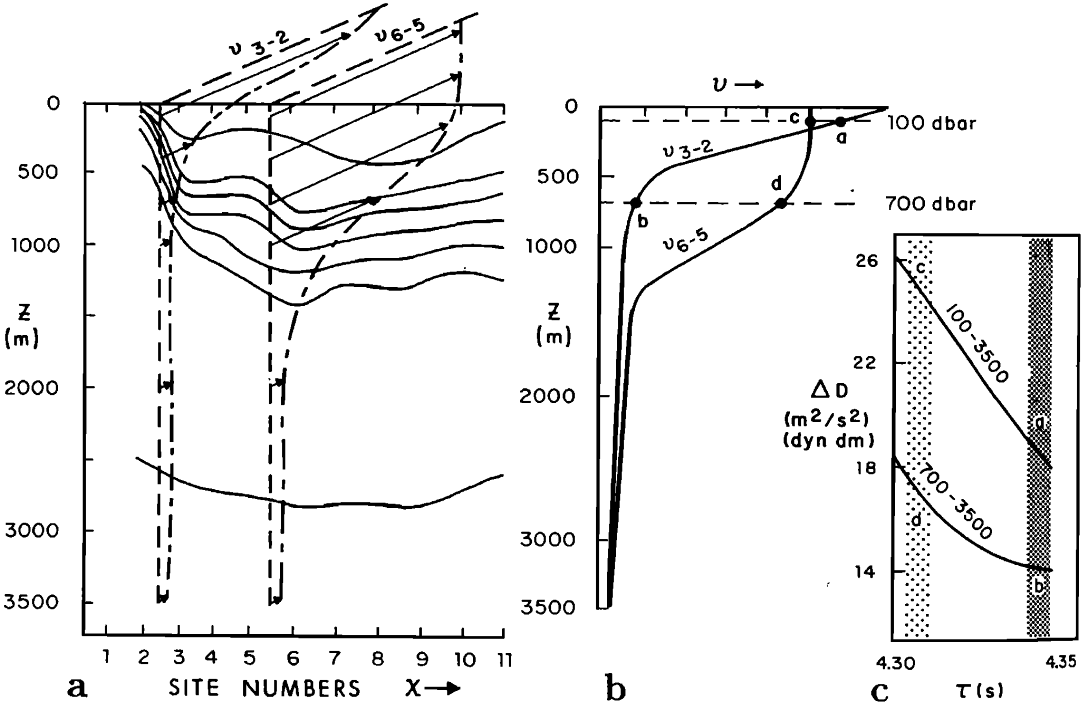

Figure 7. Schematic diagram showing how the velocity V_{IES} profiles are determined from the IES-measured τ. (a) Idealized vertical section of the pycnocline, where the cross-stream horizontal distance is indicated by "station number" or site. Vertical profiles of horizontal velocity are sketched for two locations: v_{3-2} is average between sites 2 and 3, and v_{6-5} is average between sites 5 and 6. (b) Superimposition of two velocity profiles. The v_{3-2} velocities at 100 and 700 dbar are indicated by points a and b, respectively. The v_{6-5} velocities at the same depths are indicated by points c and d. (c) $\Delta D_{100,3500}$ and $\Delta D_{700,3500}$ are shown as functions of τ. The densely shaded bar spans the two τ measured at sites 2 and 3, and the lighter bar spans the two τ measured at sites 5 and 6. The $\Delta D_{i,j}$ gradients labeled points a, b, c, and d correspond to the respectively labeled velocities in Figure 7b.

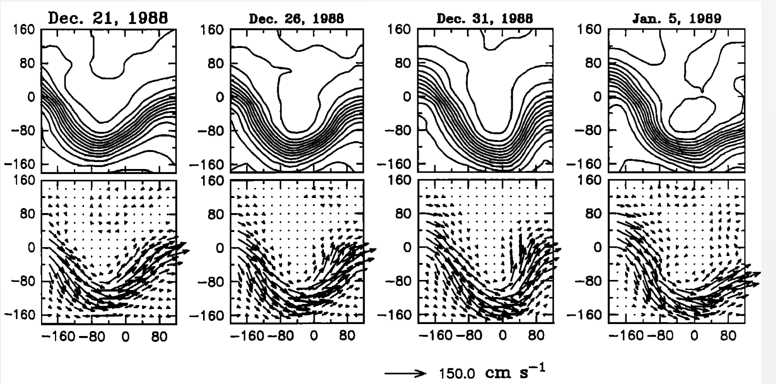

Figure 9. (a) Contoured optimal interpolation (OI) maps of $\Delta D_{400,1000}$ obtained in the SYNOP Central Array for the period December 21, 1988, to January 5, 1989. Each frame corresponds to the boxed region in Figure 8. Axes labels indicate horizontal distance in kilometers from the origin at 38°N, 68°W, where the x axis is oriented along 075°T. (b) The corresponding V_{IES} fields.

Meinen &Watts, 2000:

Vertical structure and transport on a transect across the North Atlantic Current near 42N: Time series and mean, *JGR.*

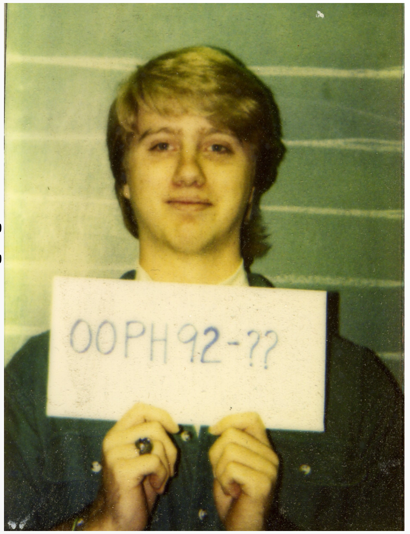

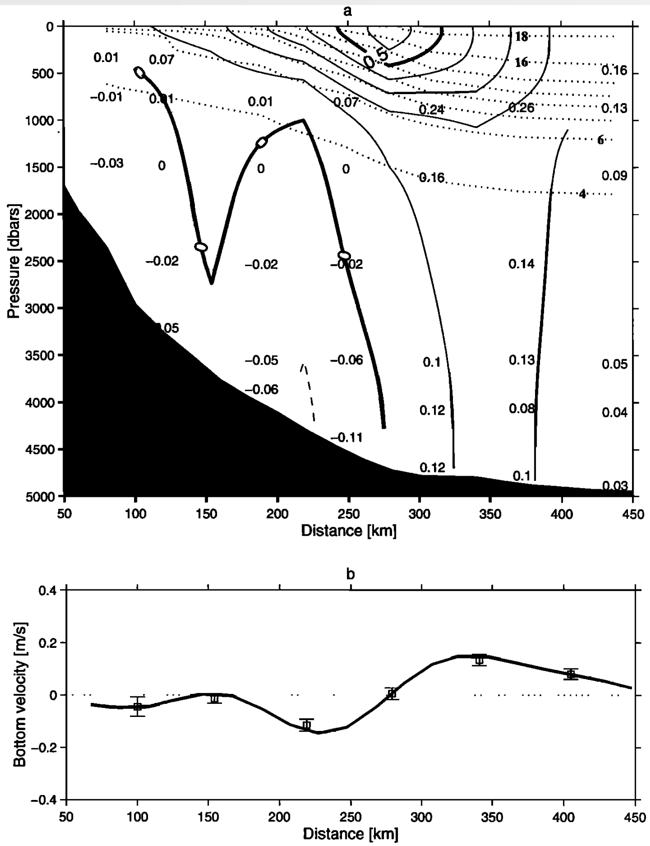

Figure 8. (a) Mean temperature section (dotted contours with small bold labels) and absolute velocity section (solid contours for velocities into the page and dashed contours for velocities out of the page). Bold solid contours indicate velocities of 0 and 50 cm s^{-1}; thin solid contours and dashed contours indicate intervals of 10 cm s^{-1}. Superimposed numbers indicate mean velocity measurements from the current meters in m s^{-1}. The averaging period is the first 6 months of the deployment, August 1993 through January 1994. (b) The mean bottom velocity from the bottom pressure maps. Squares indicate values integrated between PIES sites and are used to reference each respective V_R profile; error bars are the 1 standard deviation errors predicted by the OI procedure.

Gravest Empirical Mode (GEM) technique applied to CPIES array provides full depth maps of temperature, salinity, specific density, and absolute geostrophic velocity.

… as determined from PIES
(current meter values are listed)

Bishop, Watts & Donohue, 2008: Divergent eddy heat fluxes in the Kuroshio Extension at 144-148. Part I. Mean Structure, *JGR*

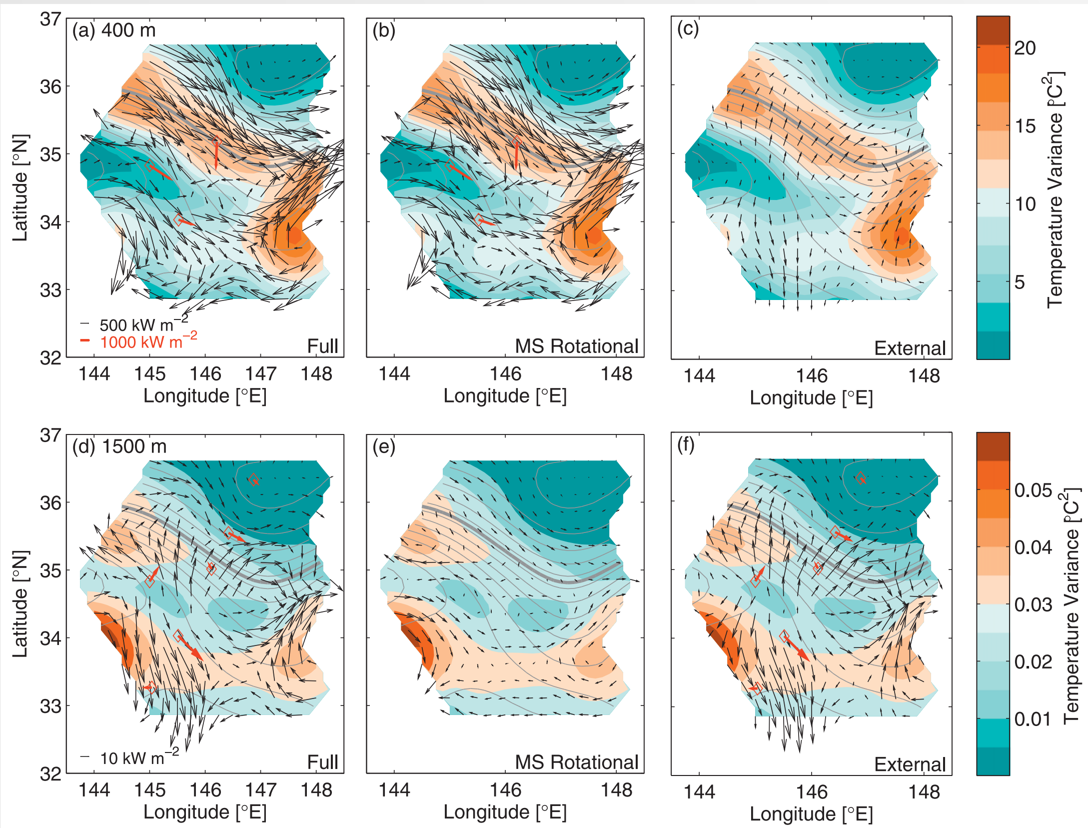

FIG. 6. External vs internal mode EHFs for the upper and deep ocean. EHF vectors superimposed on temperature variance contours (color) and 16-month mean geopotential referenced to 5300-m contours (gray) with a boldface gray contour marking the mean axis of the current. (a) 400-m total EHF vectors, (b) internal (MS rotational) EHF vectors, and (c) external EHF vectors. (d)–(f) As in (a)–(c), but for 1500 m. Red diamonds and red arrows illustrate the good agreement at the mooring locations and heat flux vectors at 250 m in (a) and (b) and at 1500 m in (d) and (f).

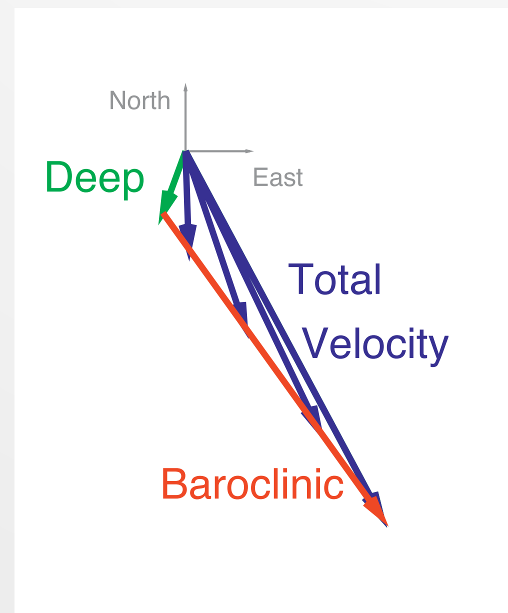

From Donohue et al. 2010

Development of the CPIES

used by more than 20 oceanographic research groups in the U.S., Canada, U.K., Germany, Norway, France, China, Korea, Japan, and Brazil.

The majority of these instruments have been built and developed by the Watts lab.

Park, Donohue, Watts, & Rainville, 2010: Distribution of deep near-inertial waves observed in the Kuroshio Extension, *JO*.

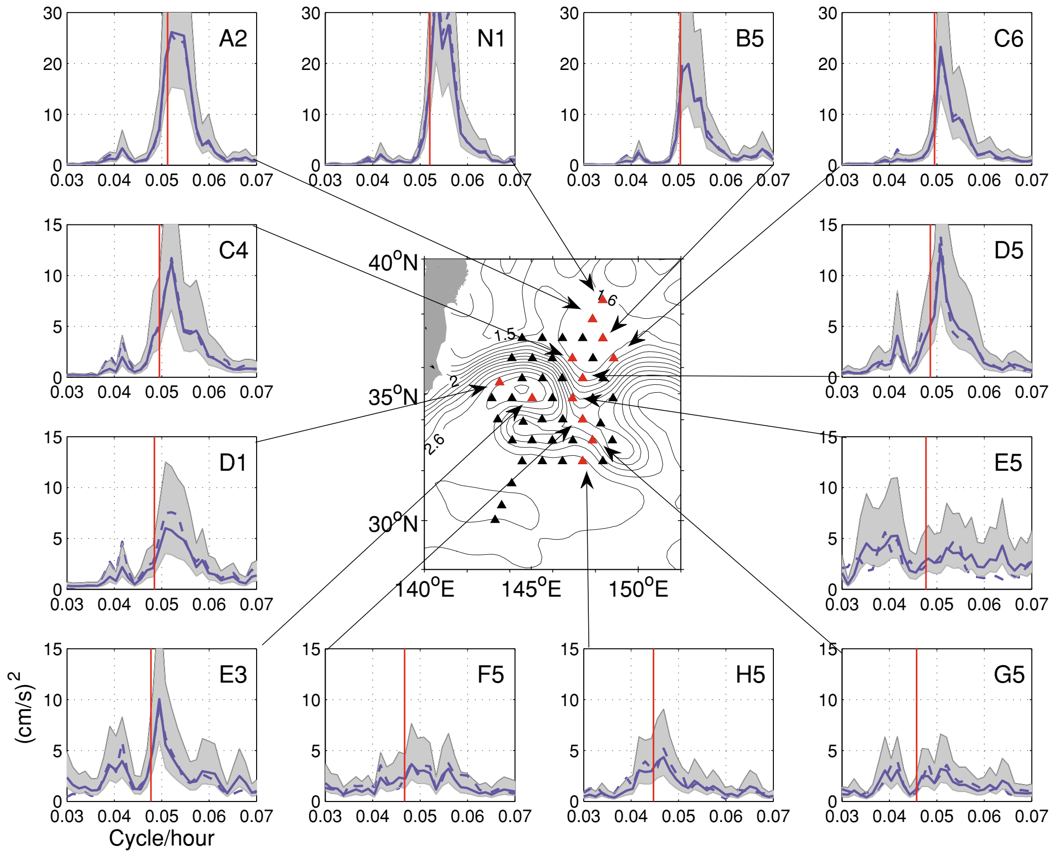

Fig. 2. Larger near-inertial energy is observed in a region north of Kuroshio than south of Kuroshio. Contours on the map show satellite-measured mean absolute dynamic topography during November 2004–April 2005. Periphery panels are variance-preserving power spectra for zonal (solid blue line) and meridional (dashed blue line) components of deep currents at twelve CPIES sites. Vertical red line and gray-shading in each power spectrum figure indicate the local Coriolis frequency and 95% confidence interval, respectively.

Principal Investigator (usually lead PI) in 14 multi-investigator field programs:

Antarctic Circumpolar Current in Drake Passage (cDrake),
Kuroshio Extension System Study (KESS),
Kuroshio in the East China Sea (ECS),
Agulhas-S Atlantic Thermohaline Transport Expt (ASTTEX),
3 Gulf of Mexico Field Programs (GOM),
Japan/East Sea (JES),
Sub-Antarctic Flux and Dynamics Experiment (SAFDE),
Labrador Sea Project,
North Atlantic Current Experiment (NAC),
Affiliated Surveys of Kuroshio off Ashizuri-Misaki (ASUKA),
Gulf Stream Synoptic Ocean Prediction (SYNOP),
Dynamics of Gulf Stream Meanders.

Andres et *al.*, 2008:

Observations of Kuroshio flow variations in the East China Sea, *JGR.*

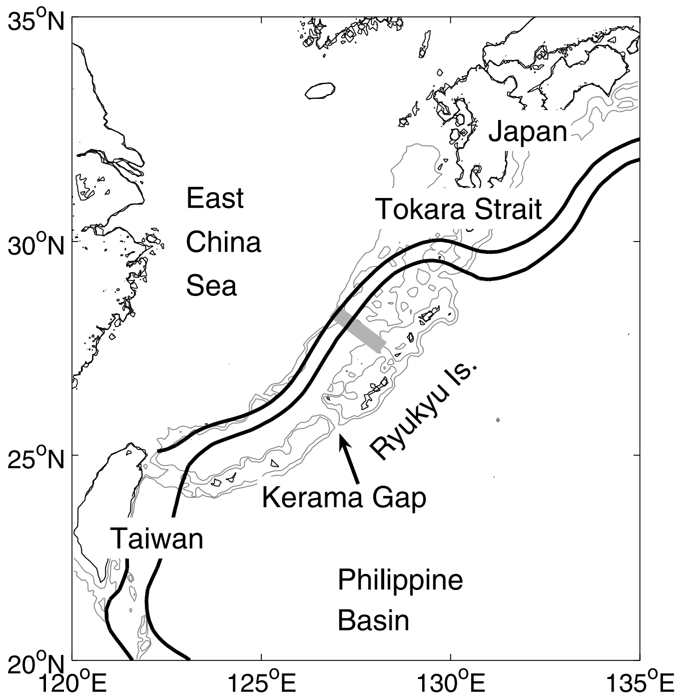

Figure 1. Regional ECS map. Kuroshio path, shown with heavy black lines, is estimated from 2002 to 2004 Mean Absolute Dynamic Topography produced by Ssalto/Duacs and distributed by AVISO with support from Cnes. Array location shown as grey rectangle. Depth contours in light grey at 500 m and 1000 m.

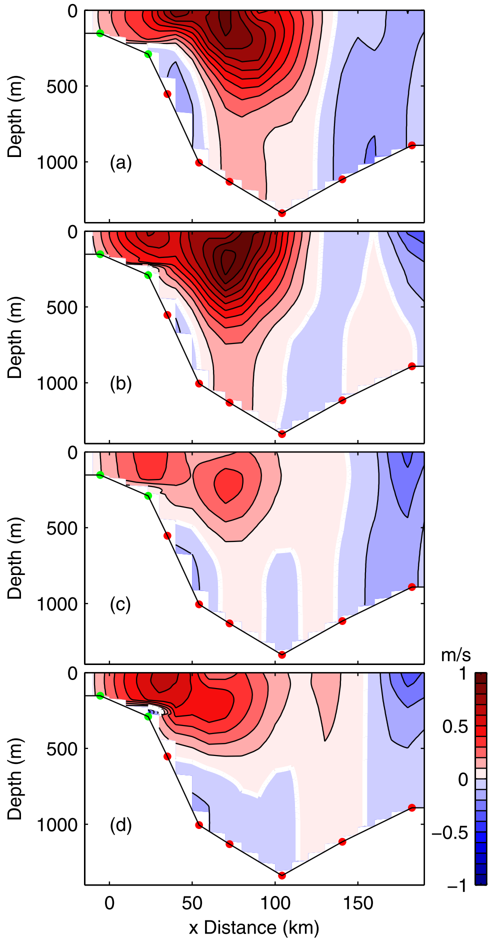

Figure 8. Velocity (y-component) snapshots. Here x = 0 at the shelf break (depth = 170 m). Green and red dots indicate locations of ADCPs and CPIESs, respectively. Contour interval is 0.1 m/s, zero contour white. (a–d) 8 March, 28 April, 5 June, and 9 September 2004, respectively.

Chereskin, Donohue, Watts, Tracey, Firing, & Cutting, 2009:

Strong bottom currents and cyclogenesis in Drake Passage, *GRL*.

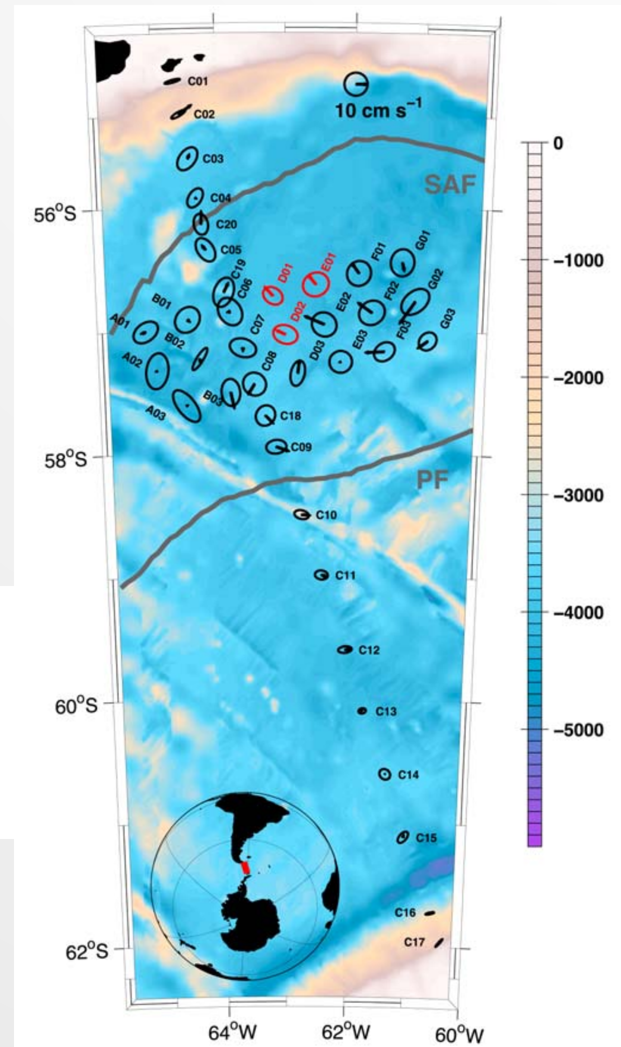

Figure 1. Record-length mean currents and standard deviation ellipses at 50 m above bottom plotted on bathymetry (m) derived from shipboard multibeam measurements and *Smith and Sandwell* [1997]. Time series from 3 recovered instruments (red) are shown in Figure 2. The mean SAF and PF (gray lines) were located following *Lenn et al.* [2008].

Kuroshio Extension Observatory (KEO) An Ocean Climate Station initiated during KESS.

http://www.pmel.noaa.gov/OCS

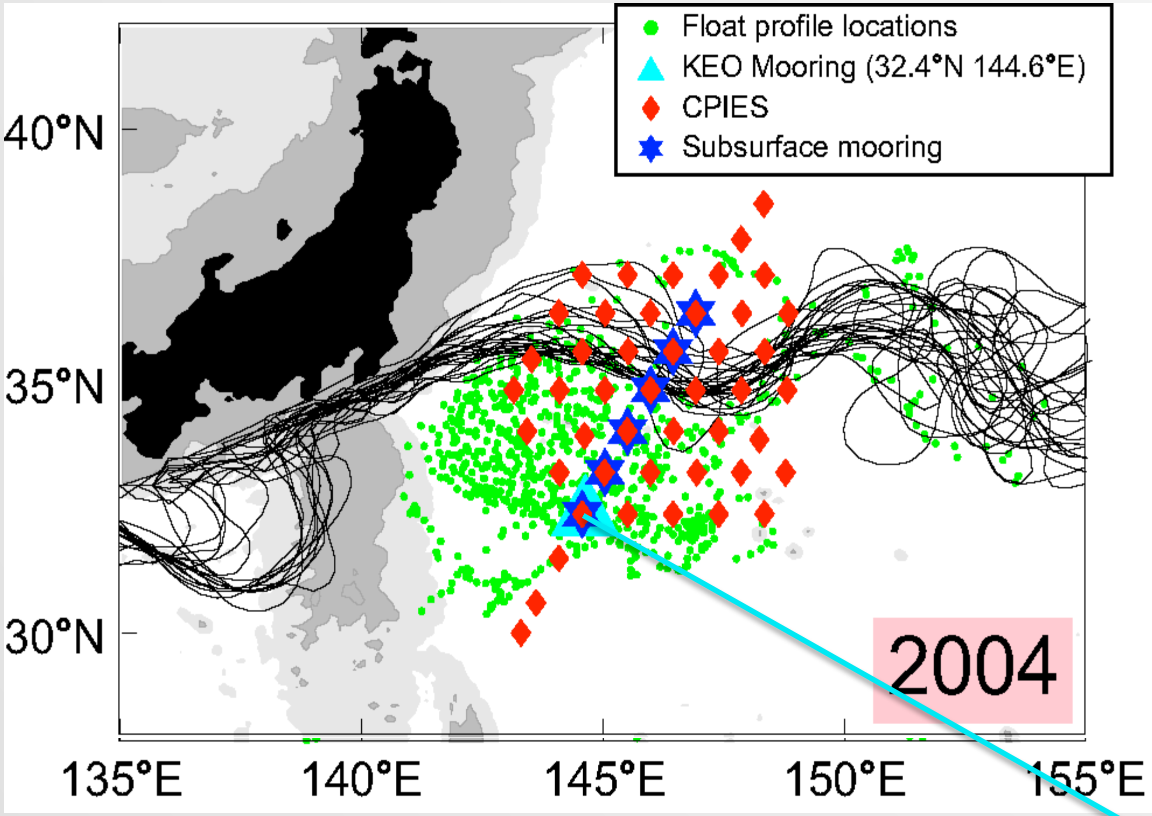

KEO – A typhoon buoy

Collaboration with Dr. Hyun-Sook Kim (NOAA NWS) for improving hurricane forecasts

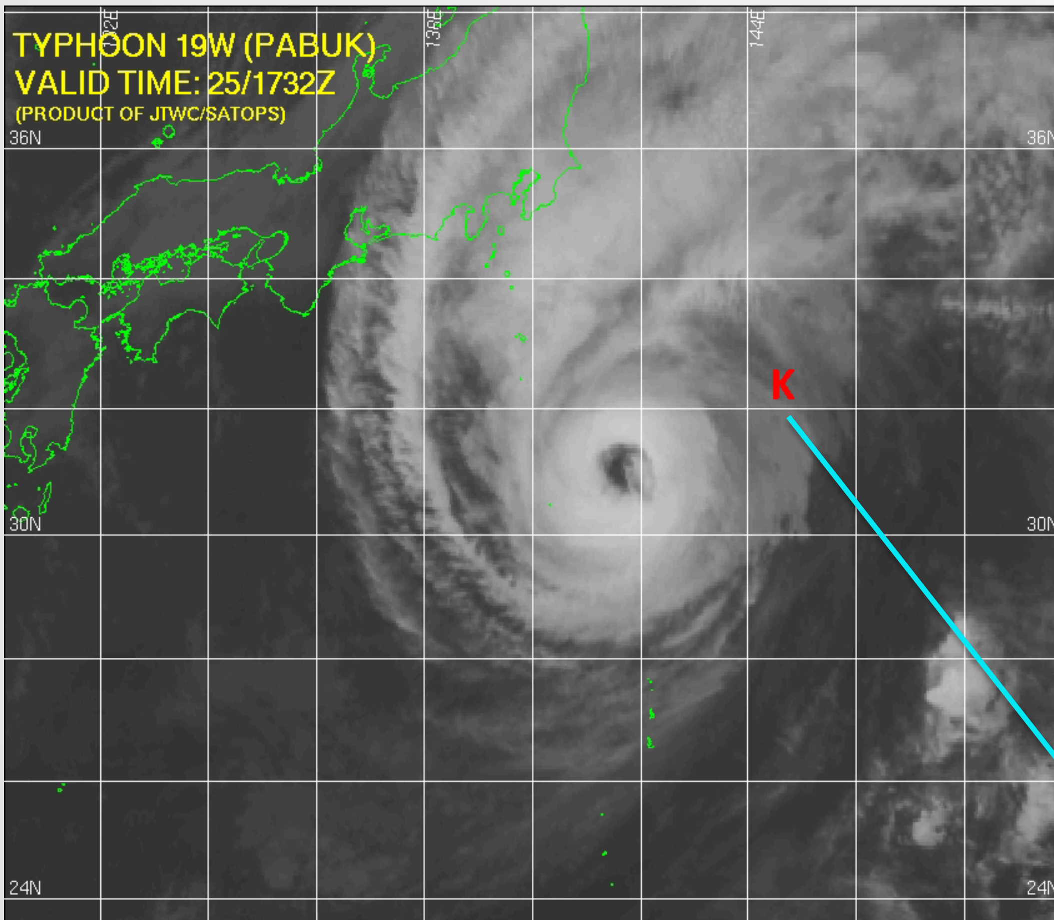

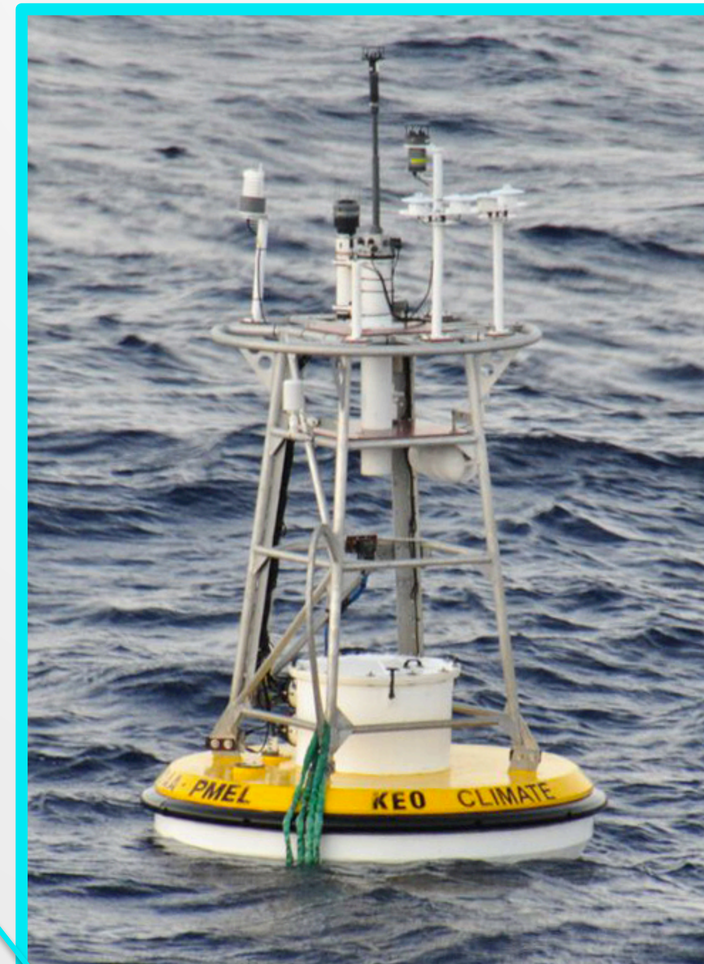

Scientific Discovery

is not a simple act, but rather
is an extended, complex process,
which culminates in a

paradigm change